Wideband Substrate-Integrated Waveguide-Fed Endfire Metasurface Antenna Array

Teng Li[ID], *Member, IEEE,* and Zhi Ning Chen[ID], *Fellow, IEEE*

Abstract—A vertically polarized substrate-integrated waveguide (SIW)-fed endfire metasurface antenna array is proposed for wideband operation. Each of the metasurfaces consists of 3 × 3 rectangular patches and is printed on the two surfaces of a single-layered substrate with a thickness of $0.16\lambda_0$ (where λ_0 is the wavelength at 32.65 GHz in free space). The antenna is fed at one side of metasurface by an open-end SIW for wideband endfire radiation. The proximity-coupled interdigital strips are introduced between the SIW and metasurface for fault-tolerant coupling. The wideband operating mechanism is revealed by studying the propagation mode and multiple resonant modes of metasurface. To verify the proposed antenna, a 1 × 4 array is presented with uniform excitation including two SIW Y junctions and an SIW T junction. Moreover, the connected SIW Y junction improved the impedance matching at the low frequencies based on the cavity mode analysis. The proposed design shows that the measured impedance bandwidth (10 dB return loss) is 26.6–38.7 GHz (37%) with the achieved gain of 9.1–13.8 dBi.

Index Terms—Antenna array, characteristic mode analysis (CMA), dispersion, endfire, leaky wave, metasurface, substrate-integrated waveguide (SIW), wideband.

I. INTRODUCTION

MILLIMETER-WAVE (mmW) communication technology is an attractive candidate for the next-generation communication system. A variety of advanced antenna techniques have been proposed, such as massive multiple-input multiple-output technology and beamforming technology for mmW systems [1]–[3]. Some of the specific applications, such as cellular phones and indoor base stations, the endfire antennas are needed to meet the desired radiation requirements [4]–[6]. At mmW bands, the substrate-integrated waveguide (SIW) should be a promising technology to realize the endfire antenna.

Many SIW-fed endfire antennas have been investigated in the literature. For the horizontally polarized (HP) one, a wide bandwidth can be realized by loading a broadband HP antenna. A dielectric rod has been employed to guide the surface wave produced by the SIW-fed Vivaldi antenna array and more than 40% bandwidth is achieved at *X*-bands [7]. Alternatively, a Vivaldi antenna array fed by a ridged SIW has been proposed with more than 75% bandwidth and efficiency, respectively [8]. By loading a bow-tie or Yagi antenna,

the HP has been achieved with a relative bandwidth of 11.6% and 25.7%, respectively [9], [10].

For the vertically polarized (VP) one, the SIW-fed horn antenna is the most popular application and has been widely studied [4]–[6], [11], [12]. However, the open end of a thin SIW (typical thickness < $\lambda_0/10$, λ_0 is a wavelength at the center frequency of operating band in the free space) is approximately equivalent to a perfect magnetic wall (PMC) and results in narrow bandwidth [13]–[15]. By loading a dielectric slab with gradually decreasing effective permittivity, 31.9% [16] and even more than 40% [17]–[19] bandwidth of SIW horn antenna are obtained where the effective permittivity can be realized by air-filled via holes with different diameters. These wideband impedance matchings are improved by using the dielectric slab transition and a relatively thick substrate (a typical thickness is $\lambda_0/3$). A $\lambda_0/4$ thick ridged SIW has been proposed for the wideband H-plane horn antenna and voltage standing wave ratio (VSWR) lower than 2.5 is obtained from 18 GHz to 40 GHz [20]. By introducing the bottom ground plane, the thickness of ridged SIW can be reduced to $0.13\lambda_0$ with VSWR below 2.5 from 6.6 to 18 GHz [21]. The ground plane can also be employed for the dielectric loading antenna and around 35.7% impedance bandwidth is achieved on $0.12\lambda_0$ thick substrate [22]. However, the introduced ground plane break the symmetry of these horn antennas and the radiation patterns in the E-plane are unsymmetrical. Another efficient method to enhance the impedance matching of thin SIW horn antenna is to load the metal strips. Two parallel plates have been proposed for matching improvement of thin SIW horn antennas (thickness < $\lambda_0/10$) with a relative bandwidth of 10% [23]. Two rows of triangle strips have been then employed instead of rectangular ones, and the shape of SIW has been optimized to improve the impedance matching as well [24]. Moreover, around 16% bandwidth is achieved based on the thin substrate (thickness < $\lambda_0/10$). Three rows of tapered-ladder triangle strips have been introduced on the $0.173\lambda_0$ thick substrate to enhance the matching and 20% bandwidth is achieved [25]. To further improve the matching of thin SIW horn antenna, the periodic parallel strips have been proposed on $0.184\lambda_0$ thick substrate with 38% bandwidth [26]. By employing the parallel strips, the SIW leaky-wave antenna has been presented with a bandwidth of more than 20% [27]. In addition, there are the other loaded structures, such as expanded copper plates [28], tapered slots [6], [29], bowl-shaped reflector [5], open parallel transition [30], directors [31], and magneto-electric dipole [4], [32], employed in the open end of SIW
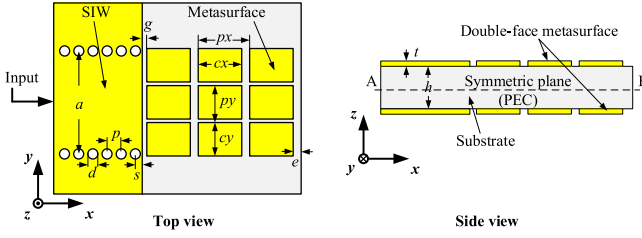
Fig. 1. Configuration of SIW-fed endfire metasurface antenna.

Fig. 2. Simulated (a) reflection coefficient and (b) normalized input impedance of SIW open end with and without metasurface.

Fig. 3. Electromagnetic characteristic of SIW-fed metasurface antenna at 30 GHz. (a) Surface current distribution. (b) E-field distributions.

to improve the impedance matching and even the radiation performance with increased thickness.

Furthermore, a variety of circularly polarized and dual-polarized structures have been investigated [33]–[40]. Some of these SIW endfire antennas still suffer from the limited bandwidth with the same problem as the VP one due to the low efficiency of VP radiation on a thin feeding substrate.

Recently, the metasurface has been employed as a radiator for broadside radiation featuring low profile and wide bandwidth [41]–[51]. The characteristic mode analysis (CMA) has been successfully used to predict the radiation behaviors of the metasurface antenna with physical insight [43]–[51]. Inspired by these works, an SIW-fed metasurface is proposed for endfire radiation with low profile, compact size, and wide bandwidth in this paper. The dispersion and characteristic mode of metasurface are analyzed to reveal the wideband operation mechanism. The proximity-coupled interdigital strips are introduced between the SIW and metasurface for the stable coupling. To verify the proposed wideband SIW-fed endfire metasurface antenna, a 1×4 array is designed, fabricated, and tested at Ka-bands. All simulations are carried out by the commercial software Computer Simulation Technology (CST) Microwave Studio.

II. ANTENNA ELEMENT

The configuration of the proposed SIW-fed endfire metasurface antenna is shown in Fig. 1. The double-surface metasurface is fed by the open-end SIW. Considering the number of resonant modes, frequencies, and simulation resource, the 3×3 rectangular patches on each side is selected which has been applied in several designs [44], [46], [48], [49], [51]. The width of SIW a is set as 5.2 mm featuring the same cutoff frequency to the standard waveguide WR-28 (7.112 mm $\times$ 3.556 mm) where $d = 0.5$ mm and $p = 0.75$ mm [52]. The higher order modes of SIW are beyond the band of interest and only the dominant mode is employed to excite the double-face metasurface. All the designs are arranged on the substrate of Rogers RT5880 with thickness of (h) 1.5 mm, $t = 0.035$ mm, $\varepsilon_r = 2.2$, and $\tan\sigma = 0.0009$. All the rectangular patches of the metasurface are designed in the same dimensions where AB is the reference plane of symmetry. The dimensions of metasurface are $py = 1.88$ mm, $cy = 1.7$ mm, $px = 2.6$ mm, and $cx = 2.2$ mm.

A. Optimization of Impedance Matching

To investigate the effect of metasurface on impedance matching, the SIW open end with and without metasurface are
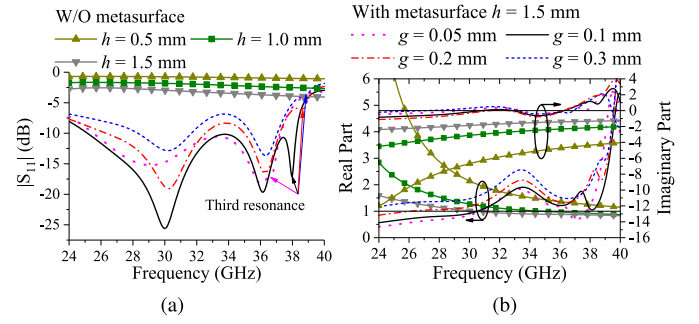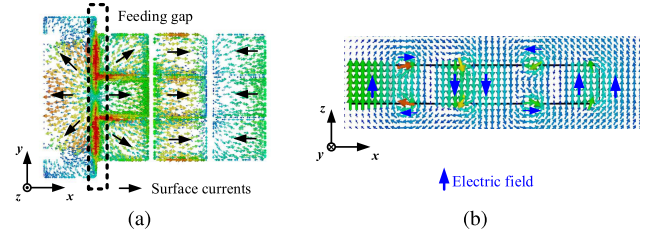
compared in Fig. 2 with varying feeding gap (g) and substrate thickness (h). As can be seen, the impedance matching is improved with the increase of h, as shown in Fig. 2(a), due to the magnitude of the real and imaginary parts of the normalized input impedance become smaller, as shown in Fig. 2(b). As a result, the thinner substrate, the higher input impedance at the SIW open end.

By loading the proposed metasurface, the impedance matching is significantly improved due to the imaginary part of the input impedance is reduced. Several impedance resonances are observed. The reflection coefficient is reduced as g decreases indicating a smaller gap is preferred for the stronger electromagnetic coupling and the lower input impedance. Considering the impedance matching over the band of interest, an optimized result is obtained at $g = 0.1$ mm, where a third impedance resonance happened at 38 GHz and accordingly broadened the impedance bandwidth. In fact, the third resonance shifts down as the feeding gap decreases, as depicted in Fig. 2(a). According to the input impedance shown in Fig. 2(b), these resonances are not the strict impedance matching points but the quasi-resonances which are the dips of $|S_{11}|$ curve. For simplicity, the $|S_{11}|$ will be subsequently used for the optimization of impedance matching for the proposed antenna.

To further investigate the effect of metasurface, Fig. 3(a) shows that most currents on the metasurface are along the x-axis at 30 GHz, therefore, the rectangular patches and gaps can be regarded as equivalent inductors and capacitors, respectively. Furthermore, the double-face metasurface allows the radiation from the gaps as shown in Fig. 3(b). The similar corresponding transmission line mode has been established in [23] and successfully applied in [24]. Therefore, there might be optimal values for the impedance matching based on this model.
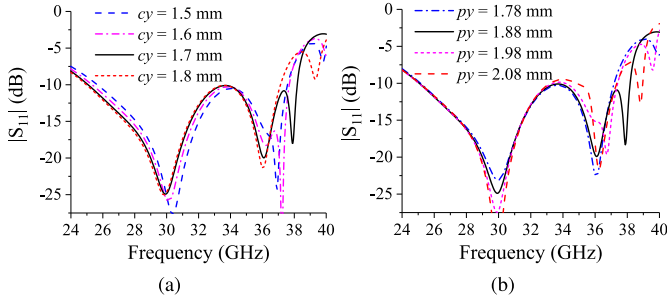
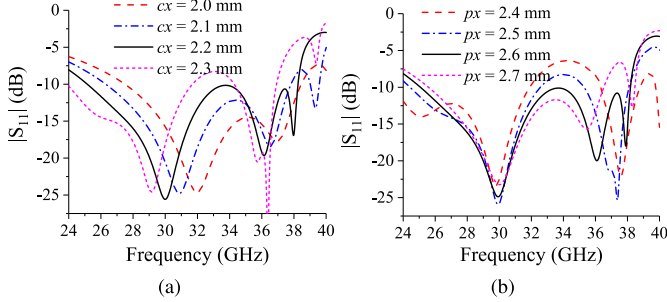Fig. 4. Simulated reflection coefficient of SIW-fed metasurface antenna with varying (a) *cy* and (b) *py*.

Fig. 5. Simulated reflection coefficient of SIW-fed metasurface antenna with varying (a) *cx* and (b) *px*.
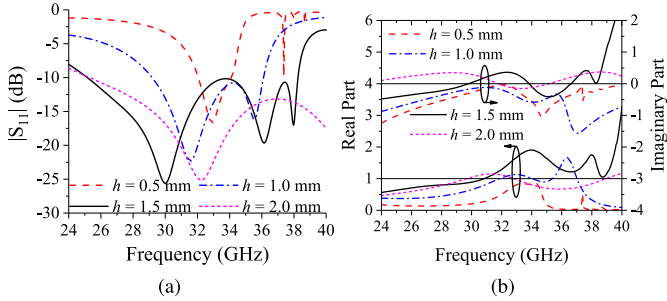

Fig. 6. Simulated (a) reflection coefficient and (b) normalized input impedance of the SIW-fed metasurface antenna with different thicknesses.

An optimization of impedance matching based on the parametric study is carried out where only one parameter is varied at a time when the others are fixed. Fig. 4(a) and (b) shows the reflection coefficient versus frequency with varying *cy* and *py*, respectively. The *cy* = 1.7 mm and *py* = 1.88 mm are optimized. Fig. 5(a) and (b) shows the reflection coefficients versus frequency with varying *cx* and *px*, respectively. The optimized *cx* = 2.2 mm and *py* = 2.6 mm are achieved with an impedance bandwidth of 25.2–38.2 GHz or 41%.

To investigate the effect of substrate thickness to the bandwidth of SIW-fed endfire metasurface antenna, another three examples with *h* = 0.5, 1.0, and 2.0 mm have been proposed for comparison, as shown in Fig. 6(a), where the configuration is the same as the original one but the dimensions are optimized. It can be found that the impedance bandwidth is rapidly reduced with the decreased substrate thickness due to the increased capacitance (imaginary part of the normalized input impedance) and decreased resistance (real part of the normalized input impedance), as shown in Fig. 6(b).
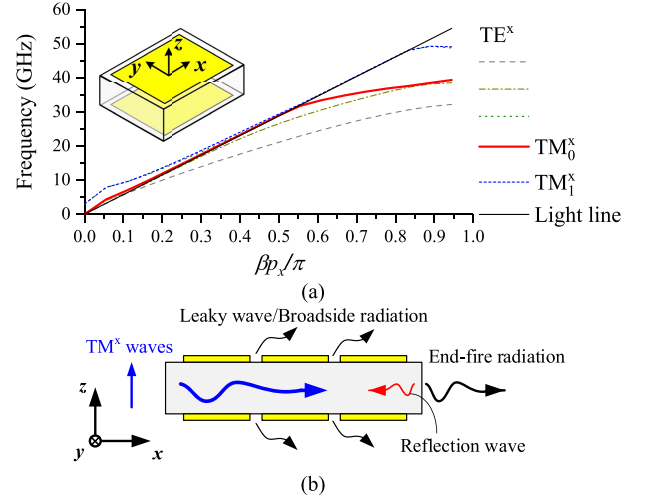

Fig. 7. Propagation wave on metasurface. (a) Dispersion curves of the proposed metasurface unit cell. (b) Propagation of TM_x waves.

B. Dispersion and Characteristic Mode Analysis of Metasurface

As mentioned earlier, most currents on the metasurface are along the *x*-axis and the broadside radiations happened at the gaps as shown in Fig. 3. Considering that the fundamental mode of SIW is quasi-TE_{10}^x where the superscript *x* denotes $E_x = 0$, and only E_z-fields exist in this paper. At the end of SIW truncation, the E_z-fields can excite the analogical TM_x wave where the $E_z \neq 0$ and the superscript *x* denotes $H_x = 0$. For the TE_x wave, only E_y-fields exist which cannot be effectively excited by the SIW open end. Therefore, it is necessary to investigate the propagation characteristic of TM_x wave on the metasurface.

The dispersion diagram of the metasurface unit cell along the *x*-axis is simulated and shown in Fig. 7(a). It is found that the TM_x^0 wave is a leaky wave before 30 GHz and then becomes a slow wave. The other higher order modes of TM_x waves, such as TM_x^1 wave, are leaky waves over the operating band or beyond the operating band. Therefore, the TM_x^0 wave should be mainly taken into account.

For the proposed metasurface, there are only three periodic elements along the *x*-axis and the incident TM_x^0 wave cannot be fully leaked from the broadside based on the leaky-wave mode while still less the slow wave mode. Although increasing the element number will improve the leakage, the size of metasurface will be significantly increased. For purpose of compactness, the element number is fixed to be three, therefore, the partial TM_x^0 wave will be propagated along the *x*-axis to the end. At the end of the metasurface, the most of the TM_x^0 waves are directly radiated, while the others are reflected due to the truncation, as shown in Fig. 7(b). The standing wave accordingly happens between the SIW open end and the metasurface truncation. Therefore, it is necessary to investigate the resonant behaviors of metasurface based on the TM_x^0 wave over the band of interest. Considering that there is only E_z-field for the TM_x^0 wave and the metasurface is symmetrical about the plane *AB*, as shown in Fig. 1, only the upper half part is taken account of by employing the image theory and the simplified model is presented in Fig. 8.
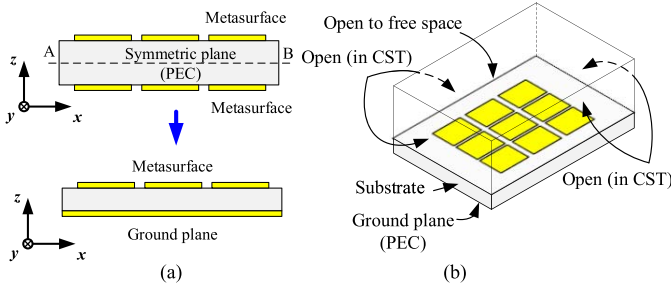
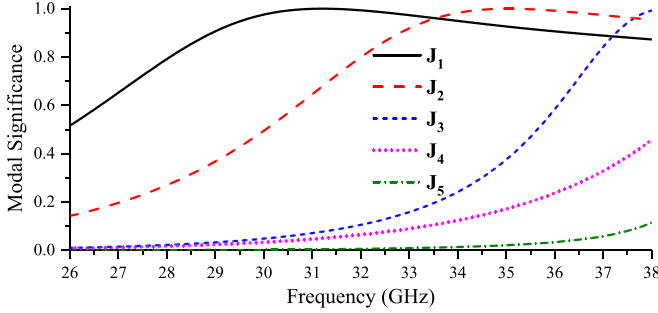Fig. 8. Simplification of double-face metasurface. (a) Simplification. (b) Simulation setup of CMA in CST.

Fig. 9. MSs of selected modes.

Fig. 10. Modal currents, E-fields, and radiation patterns of modes J_1–J_5 for the simplified metasurface.

Fig. 11. Normalized modal weighting coefficient, gain, and total radiation patterns of the proposed SIW-fed endfire metasurface antenna element.

To predict the resonant modes of metasurface, the theory of characteristic mode is employed and carried out by CST. The modal weighting coefficients (α_n) characterizes the contribution of mode J_n to the total currents [53]

$$\alpha_n = 1/(1 + j\lambda_n)\int J_n \cdot E_i \, dS \quad (1)$$

where the λ_n is the eigenvalue of mode J_n, E_i is the impressed electric field (E-field), and S is the surface of conductor area. The modal significance (MS) and the modal excitation coefficient are defined as

$$\text{MS} = 1/|1 + j\lambda_n| \quad (2)$$

$$V_i = \int J_n \cdot E_i \, dS. \quad (3)$$

Considering the E-fields shown in Fig. 3(b), the modes J_1–J_5 including J_x (the current component along the x-axis) are selected for investigation according to (3), and the other modes are ignored.

The MSs of selected modes over 26–38 GHz are calculated and sorted at 32 GHz, as shown in Fig. 9. Modes J_1, J_2, and J_3 resonate at 31, 35, and 38 GHz, respectively, where the modal currents, E-fields, and radiation pattern (in a half-space) at resonant frequencies are depicted in Fig. 10. As can be seen, the modes J_1, J_2, and J_3 are quasi-TM$_{10}$, quasi-TM$_{20}$, and quasi-TM$_{30}$ modes, respectively, with the corresponding one, two and three beams. For Modes J_4 and J_5, the resonant frequencies are both beyond the band of interest and the modal currents at 38 GHz are accordingly depicted in Fig. 10 as well. The observed edged and inversed E-fields indicate the increased sidelobe or split beams in the xy plane (H-plane) as shown in Fig. 10.

Due to the multiple characteristic modes, the reflected waves are radiated from the broadside and the impedance matching
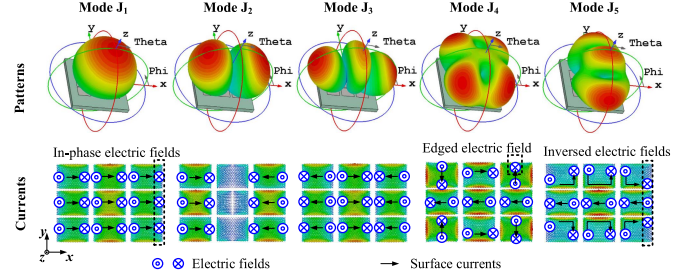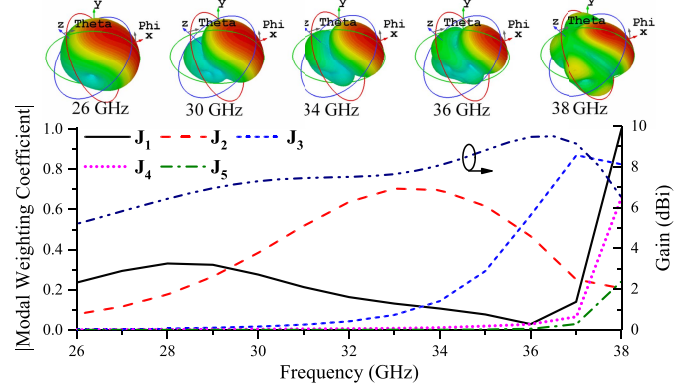
is improved accordingly. To investigate the contribution of each mode for the broadside radiation, the modal weighting coefficients are calculated according to (1), as shown in Fig. 11 where the radiation patterns and gain curve over frequency are also depicted. It is found that modes J_1, J_2, and J_3 take effect by turns over 26–37 GHz. Then, all the modes mixed at 38 GHz with the gain drop. The simulated gain is within 5.2–9.5 dBi over 26–38 GHz.

Over 26–29 GHz, the mode J_1 plays a major role in the broadside resonant radiation but with a small $|\alpha_1|$ due to the leaky-wave operation before 30 GHz. The endfire radiation pattern without any sidelobe in the E-plane is achieved in accord with the pattern of J_1. Then, the mode J_2 dominates the resonant radiation before 36 GHz with a large $|\alpha_2|$ because the leaky-wave radiation becomes weaker. Two inversed beams along the x-axis are observed in accord with the pattern of J_2. Mode J_3 becomes visible after 34 GHz and plays a major role after 36 GHz with a larger $|\alpha_3|$ where the additional sidelobes appear along the z-axis in accord with the pattern of J_3.

With the decreased leaky wave, the reflected wave becomes stronger and the $|\alpha_1|$ abnormally fast increase after 37 GHz indicating a broad beam in the E-plane. Furthermore, the modes J_4 and J_5 take effect on the total radiation pattern as well. The total radiation pattern and gain drop of metasurface antenna at 38 GHz are accordingly achieved, as shown in Fig. 11, where the radiation results are obtained by the full-wave simulations.

As a result, the wideband behavior of the proposed endfire antenna is mainly attributed to the leaky-wave radiation at the broadside and endfire radiation at the truncation, furthermore, improved by the multimode resonant broadside radiation of
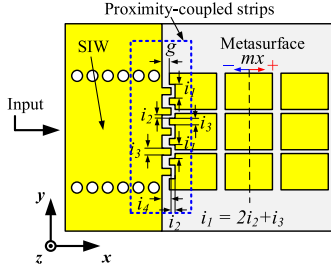
Fig. 12. Proposed proximity-coupled feeding strips for the SIW-fed endfire antenna element.
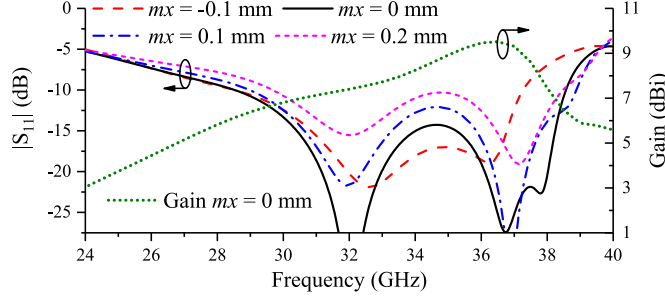

Fig. 13. Simulated gain and reflection coefficients of the proposed proximity-coupled antenna with varying *mx*.

the metasurface with the increased beamwidth and sidelobe level (SLL). Therefore, there is no clear correspondence between the three impedance resonances and the five characteristic modes of metasurface. The metasurface actually works as a radiator and transition between the SIW and free space.

C. Proximity-Coupled Feeding

The obtained impedance matching is quite critical and sensitive to the feeding gap, as shown in Fig. 2. Any fabrication errors might cause impedance mismatching. Therefore, an effective feeding structure is required to improve the stability of impedance matching over the band of interest and against the fabrication tolerance. To maintain the strong electromagnetic coupling with a larger feeding gap between the SIW and metasurface, a proximity-coupled feeding structure similar to an interdigital capacitor is proposed as shown in Fig. 12. Five feeding strips are inserted into the metasurface with a small gap of $i_2 = 0.18$ mm. The width and the length of the strips are simply supposed to be equal. The feeding gap is fixed at $g = 0.2$ mm and $i_1 = 2i_2 + i_3$. The other parameters are optimized based on the method of parametric study where $i_3 = 0.3$ mm and $i_4 = 0.43$ mm are obtained.

Fig. 13 shows the optimized impedance matching over the frequency with varying *mx* (*mx* is the position error of metasurface along the *x*-axis caused by fabrication, as shown in Fig. 12). As can be seen, the obtained 10 dB impedance bandwidth is 28.5–38.5 GHz or 30% with an achieved gain of 6.1–9.5 dBi. The reflection around 35 GHz is less than -14 dB, and the bandwidth of 30–38 GHz is still available within -0.1 mm $\leq mx \leq 0.2$ mm which indicates a more flexible tolerance than the initial one.

III. ANTENNA ARRAY

A. Feeding Network

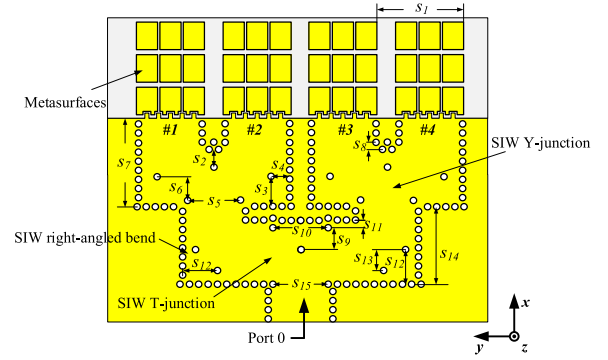To verify the proposed antenna and increase the gain, a 1×4 array is designed as shown in Fig. 14 where two

Fig. 14. Top view of the proposed 1×4 array.

TABLE I
DIMENSIONS OF FEEDING NETWORK AND TRANSITION (UNIT: mm)

Parameter	Value	Parameter	Value	Parameter	Value
s_1	7.00	s_{10}	4.38	t_4	0.40
s_2	0.60	s_{11}	0.58	t_5	2.83
s_3	2.40	s_{12}	2.87	t_6	0.75
s_4	1.53	s_{13}	1.73	t_7	2.37
s_5	4.27	s_{14}	6.33	t_8	1.68
s_6	1.92	s_{15}	4.48	t_9	2.78
s_7	7.15	t_1	2.03	t_10	0.60
s_8	0.60	t_2	6.23	t_11	7.112
s_9	1.81	t_3	0.40	t_12	3.556
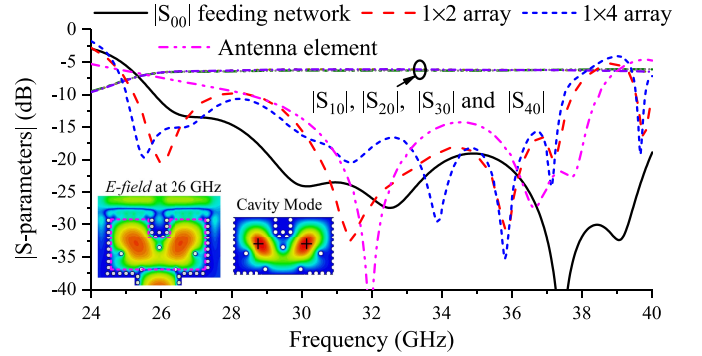
Fig. 15. Simulated S-parameters of antenna element, array and feeding network including E-field distribution of 1×2 array and corresponding cavity mode of even TE_{210} mode.

SIW Y junctions, two right-angled bends, and an SIW T junction are connected as the feeding network with equal outputs. The detailed dimensions are summarized in Table I.

The performance of the feeding network is shown in Fig. 15 where a bandwidth of 26–38 GHz is obtained with equal outputs. The impedance matching of the 1×4 array with a feeding network is depicted in Fig. 15 as well where the reflection coefficients of a single antenna and a 1×2 array feeding by an SIW Y junction are depicted for comparison.

Comparing with the single antenna, the impedance bandwidths of arrays are deteriorated around 38 GHz but improved the low frequencies. The improvements are mainly attributed to the SIW Y junction which is operating in an even TE_{210} cavity mode around 26 GHz as depicted in Fig. 15. With this modal behavior, the impedance bandwidth of 25–37.5 GHz is achieved for the antenna array.

(a)   (b)

(c)

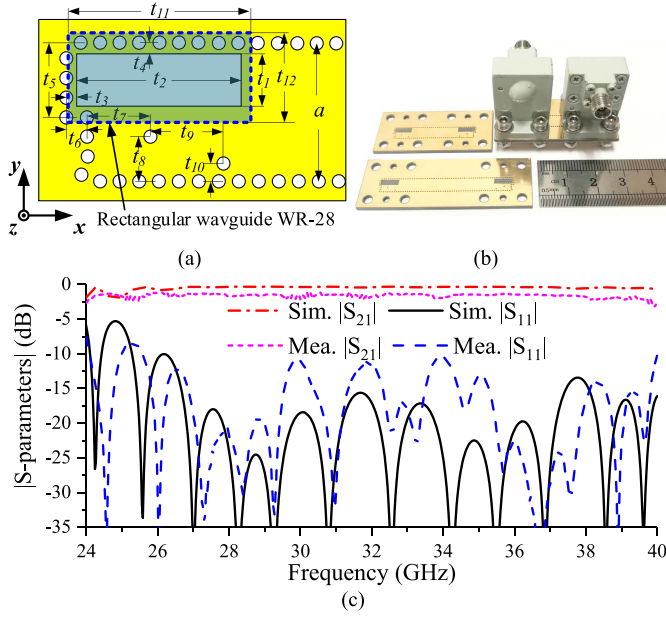Fig. 16. Configuration and S-parameters of the proposed transition. (a) Top view. (b) Fabricated two back-to-back prototypes. (c) Simulated and measured S-parameters of the longer prototype.

B. Transition Between SIW and Rectangular Waveguide

In order to connect the proposed antenna into the measurement systems, a wideband right-angled transition between SIW and rectangular waveguide (RWG) is required. A variety of right-angled transitions have been investigated in the literature, but the bandwidth is limited [54], [55]. By using a ridged flange between the SIW and RWG, the bandwidth is improved to cover the full Ka-band [56] or even up to 54.67% [57]. A simple transition without additional flange has been proposed to cover full Ka-band using three slots and a metallic via [58]. Inspired by this paper, the transition is simplified by using a single slot and two vias to cover the band of interest, as shown in Fig. 16(a).

Two back-to-back prototypes with different lengths are fabricated and tested as shown in Fig. 16(b). The measured and simulated S-parameters of the longer prototype are depicted in Fig. 16(c) and good agreements are observed. The measured impedance bandwidth with $|S_{11}| < -10$ dB ranges from 25.6 to 40 GHz with the measured $|S_{21}|$ is within 1.6 ± 0.5 dB. Comparing with the results of the short prototype, the calculated average insertion loss for a single transition is 0.75 dB suitable for the subsequent measurements.

IV. MEASUREMENTS AND DISCUSSION

To verify the proposed endfire array, a prototype with a dimension of 28 mm × 40 mm is fabricated as shown in Fig. 17. Fig. 18 shows the simulated and measured impedance matchings of the proposed array antenna. The measured −10 dB bandwidth is from 26.6 to 38.7 GHz with a fractional bandwidth of 37% which is slightly less than the simulated bandwidth of 39%. The differences might be caused by the fabrication errors and the alignment errors between SIW and RWG.

The simulated and measured gain of the proposed antenna array as a function of the frequency is plotted in Fig. 18
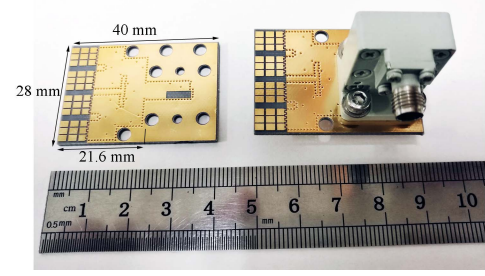
Fig. 17. Photography of the fabricated SIW-fed endfire metasurface antenna array.
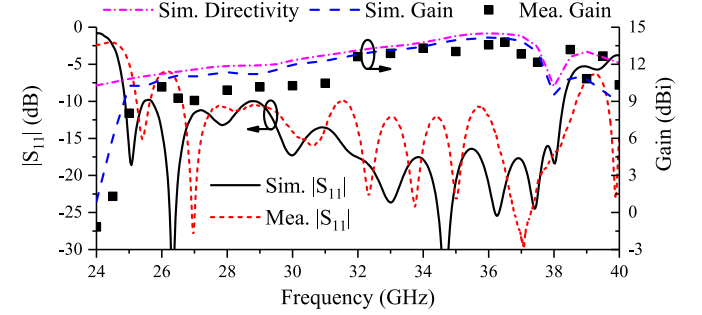
Fig. 18. Simulated and measured reflection coefficient and gain of the proposed metasurface antenna array.

(a)   (b)

(c)   (d)
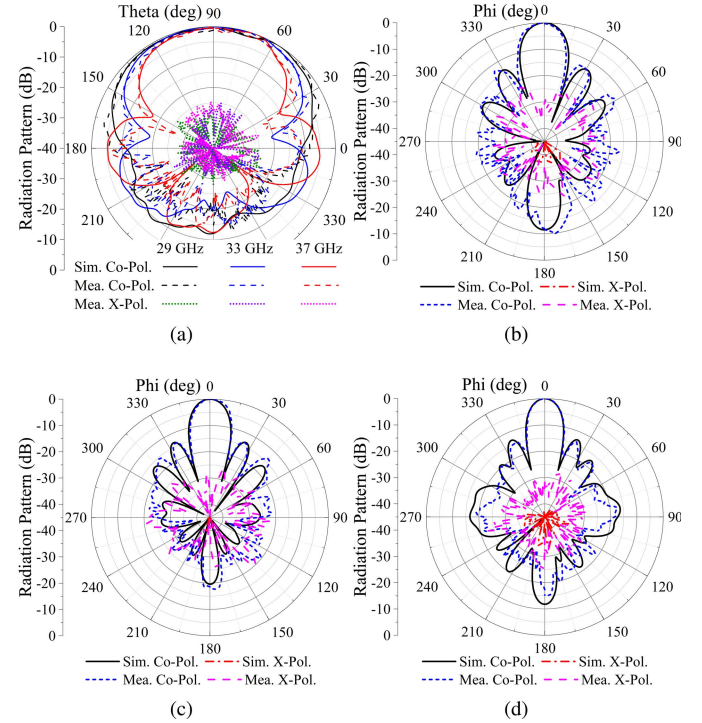
Fig. 19. Simulated and measured (a) E-plane ($\phi = 0°$) and H-plane ($\theta = 90°$) radiation patterns of the proposed metasurface antenna array at (b) 29, (c) 33, and (d) 37 GHz.

as well. From 32 GHz to 37.5 GHz, good agreements are obtained between simulation and measurements showing a measured gain of 12.2–13.8 dBi. The measured gain is higher than the simulated one around 38.5 GHz and close to the simulated directivity which can be attributed to the improved impedance matching.

TABLE II
COMPARISON WITH OTHER ENDFIRE VERTICALLY POLARIZED ANTENNAS

Antennas	f_c (GHz)	Bandwidth (%)	Peak Gain (dBi)	Size($\lambda \times \lambda$)	Thickness (λ)	Type
[4]	60	44/16.4*	6/12*	0.57×0.34	0.47	SIW-Fed Magnetoelectric
[6]	27	>34.9	9.6	0.5×1.35	1.1	SIW-Fed Tapered Slot
[16]	20	31.9	8	1.47×3.77	0.27	SIW Horn-Fed Dielectric Slab
[18]	22.15	41.1	8.3	0.78×1.33	0.32	SIW-Fed Dielectric Slab
[22]	22.86	35.7	8.9	1.52×2.63	0.12	Semi-Open SIW Horn
[24]	14.8	16	7.1	1.26×1.56	0.1	SIW Horn-Fed Strips
[25]	34	20	11	2.3×4.4	0.17	Gap SIW Horn-Fed Strips
[26]	36.15	38	14.8	2.82×2.89	0.18	SIW Horn-Fed Strips
[32]	33	44	12	2.6×3.8	0.5	SIW Horn-Fed Dipole Array
Element 1**	**31.7**	**41**	**9.5**	**0.58×0.85**	**0.16**	**SIW-Fed Metasurface**
Element 2**	**33.5**	**30**	**9.5**	**0.61×0.89**	**0.17**	**SIW-Fed Metasurface**
1×4 Array	**32.65**	**37**	**13.8**	**2.35×3.05**	**0.16**	**SIW-Fed Metasurface**

f_c denotes the center frequency. * Array. ** By simulation. Elements 1 is the proposed original metasurface antenna element. Element 2 is the proposed metasurface antenna element with proximity-coupled feeding.

The measured gain curve has a similar shape to the simulated one over the low frequencies (lower than 32 GHz). However, the obtained gain is reduced to 9.1–10.5 dBi which is 1.8 dB less than the simulations over 27–31 GHz. Considering that the beamwidth of antenna element at the low frequencies is much wider than the high frequencies as depicted in Fig. 11, indicating a lower directivity and more sensitive to the surroundings. Therefore, the patterns at the low frequencies are distorted by the connected coaxial adapter and mounting bracket where the gain is then reduced. The simulated and measured E-plane radiation patterns of the proposed antenna array at 29, 33, and 37 GHz are plotted in Fig. 19(a). As can be seen, the measured pattern decreased at $\theta = 90°$ and results in the reduced gain. On the other hand, the beams at the high frequencies are more focused along the x-axis indicating less sensitive to the surroundings. Therefore, the measured gains at 33 GHz and 37 GHz are more close to the simulations. Due to the multimode operation of the proposed metasurface, the simulated half-power beamwidth (HPBW) in the E-plane changes from 133° to 79° over 27–37 GHz. The measured cross-polarization levels are below −25 dB, and the simulated ones are less than −40 dB. The obtained back lobe levels are below −13 dB which is close to the simulated −12.4 dB.

Fig. 19(b)–(d) shows the H-plane patterns of the antenna array at 29, 33, and 37 GHz. As can be seen, the measured patterns agree well with the simulations. The measured SLLs are around −13 dB. The simulated HPBW of 14°–19° in the H-plane is more stable than in the E-plane over 27–37 GHz due to the formed metasurface antenna array. The obtained cross-polarization levels are less than −25 dB over the HPBW of the main beam and the simulated ones are still below −40 dB. The measured back lobe levels are less than −10, −17, and −15 dB at 29, 33, and 37 GHz, respectively.

Table II summarized the performance of the endfire VP antennas. Obviously, the proposed metasurface antennas have a lower profile than those in [4], [6], [16], [18], and [26] while still maintaining a comparable bandwidth. The semiopen SIW horn is wideband and low profile but the pattern in the E-plane is asymmetric [22]. Compared with the SIW horn-fed strips antenna [24]–[26], the proposed metasurface antennas

have a wider or comparable bandwidth with similar thickness. Furthermore, the compact size of the metasurface antenna element enables it more flexible for various applications.

V. CONCLUSION

A wideband SIW-fed endfire metasurface antenna array has been proposed and verified. The metasurface has been employed as a transition and a multimode radiator for bandwidth broadening. A proximity-coupled structure has been proposed for stable coupling between metasurface and SIW open end. The double-surface metasurface has been optimized for wideband operation, and the modal behaviors have been investigated based on the theory of characteristic modes to reveal the operating mechanism. A 1×4 metasurface antenna array has been presented as an example for the VP endfire application and verified by the measurement. The CMA has been employed to reveal the operating mechanism of the proposed antenna and can be used for further studies, such as control of SLL by suppressing the higher order modes with modified unit cells [48]. This type of antenna and array features a low profile and wide bandwidth suitable for the applications in communication and radar systems.

REFERENCES

[1] A. L. Swindlehurst, E. Ayanoglu, P. Heydari, and F. Capolino, "Millimeter-wave massive MIMO: The next wireless revolution?" *IEEE Commun. Mag.*, vol. 52, no. 9, pp. 56–62, Sep. 2014.

[2] W. Roh *et al.*, "Millimeter-wave beamforming as an enabling technology for 5G cellular communications: Theoretical feasibility and prototype results," *IEEE Commun. Mag.*, vol. 52, no. 2, pp. 106–113, Feb. 2014.

[3] Y. Kim *et al.*, "Feasibility of mobile cellular communications at millimeter wave frequency," *IEEE J. Sel. Topics Signal Process.*, vol. 10, no. 3, pp. 589–599, Apr. 2016.

[4] Y. Li and K.-M. Luk, "A multibeam end-fire magnetoelectric dipole antenna array for millimeter-wave applications," *IEEE Trans. Antennas Propag.*, vol. 64, no. 7, pp. 2894–2904, Jul. 2016.

[5] L. Ge, K. M. Luk, and S. Chen, "360° beam-steering reconfigurable wideband substrate integrated waveguide horn antenna," *IEEE Trans. Antennas Propag.*, vol. 64, no. 12, pp. 5005–5011, Dec. 2016.

[6] B. Yang, Z. Yu, Y. Dong, J. Zhou, and W. Hong, "Compact tapered slot antenna array for 5G millimeter-wave massive MIMO systems," *IEEE Trans. Antennas Propag.*, vol. 65, no. 12, pp. 6721–6727, Dec. 2017.

[7] R. Kazemi, A. E. Fathy, and R. A. Sadeghzadeh, "Dielectric rod antenna array with substrate integrated waveguide planar feed network for wideband applications," *IEEE Trans. Antennas Propag.*, vol. 60, no. 3, pp. 1312–1319, Mar. 2012.

[8] R. Kazemi and A. E. Fathy, "16-element Vivaldi antenna array fed by a single ridge substrate integrated waveguide with over 75% bandwidth," in *IEEE MTT-S Int. Microw. Symp. Dig.*, Jun. 2014, pp. 1–4.

[9] A. Dadgarpour, B. Zarghooni, B. S. Virdee, and T. A. Denidni, "Millimeter-wave high-gain SIW end-fire bow-tie antenna," *IEEE Trans. Antennas Propag.*, vol. 63, no. 5, pp. 2337–2342, May 2015.

[10] X. Zou, C.-M. Tong, J.-S. Bao, and W.-J. Pang, "SIW-fed Yagi antenna and its application on monopulse antenna," *IEEE Antennas Wireless Propag. Lett.*, vol. 13, pp. 1035–1038, 2014.

[11] H. Wang, D.-G. Fang, B. Zhang, and W.-Q. Che, "Dielectric loaded substrate integrated waveguide (SIW) H-plane horn antennas," *IEEE Trans. Antennas Propag.*, vol. 58, no. 3, pp. 640–647, Mar. 2010.

[12] L. Gong, K. Y. Chan, and R. Ramer, "Substrate integrated waveguide H-plane horn antenna with improved front-to-back ratio and reduced sidelobe level," *IEEE Antennas Wireless Propag. Lett.*, vol. 15, pp. 1835–1838, Mar. 2016.

[13] L. Wang, X. Yin, S. Li, H. Zhao, L. Liu, and M. Zhang, "Phase corrected substrate integrated waveguide H-plane horn antenna with embedded metal-via arrays," *IEEE Trans. Antennas Propag.*, vol. 62, no. 4, pp. 1854–1861, Apr. 2014.

[14] D. Sun, J. Xu, and S. Jiang, "SIW horn antenna built on thin substrate with improved impedance matching," *Electron. Lett.*, vol. 51, no. 16, pp. 1233–1235, Aug. 2015.

[15] L. Sun, B. Sun, J. Yuan, W. Tang, and H. Wu, "Low-profile, quasi-omnidirectional substrate integrated waveguide (SIW) multihorn antenna," *IEEE Antennas Wireless Propag. Lett.*, vol. 15, pp. 818–821, 2016.

[16] Y. Cai *et al.*, "Compact wideband SIW horn antenna fed by elevated-CPW structure," *IEEE Trans. Antennas Propag.*, vol. 63, no. 10, pp. 4551–4557, Oct. 2015.

[17] Y. Cai, Z.-P. Qian, Y.-S. Zhang, J. Jin, and W.-Q. Cao, "Bandwidth enhancement of SIW horn antenna loaded with air-via perforated dielectric slab," *IEEE Antennas Wireless Propag. Lett.*, vol. 13, pp. 571–574, 2014.

[18] Y. Cai, Z. Qian, Y. Zhang, and W. Cao, "A compact wideband SIW-fed dielectric antenna with end-fire radiation pattern," *IEEE Trans. Antennas Propag.*, vol. 64, no. 4, pp. 1502–1507, Apr. 2016.

[19] Y. Cai, Y. Zhang, Z. Qian, W. Cao, and L. Wang, "Design of compact air-vias-perforated SIW horn antenna with partially detached broad walls," *IEEE Trans. Antennas Propag.*, vol. 64, no. 6, pp. 2100–2107, Jun. 2016.

[20] A. R. Mallahzadeh and S. Esfandiarpour, "Wideband H-plane horn antenna based on ridge substrate integrated waveguide (RSIW)," *IEEE Antennas Wireless Propag. Lett.*, vol. 11, pp. 85–88, 2012.

[21] Y. Zhao, Z. Shen, and W. Wu, "Wideband and low-profile H-plane ridged SIW horn antenna mounted on a large conducting plane," *IEEE Trans. Antennas Propag.*, vol. 62, no. 11, pp. 5895–5900, Nov. 2014.

[22] Y. Cai, Y. Zhang, L. Yang, Y. Cao, and Z. Qian, "A low-profile wideband surface-mountable substrate-integrated waveguide horn antenna," *IEEE Antennas Wireless Propag. Lett.*, vol. 16, pp. 2730–2733, 2017.

[23] M. Esquius-Morote, B. Fuchs, J. F. Zürcher, and J. R. Mosig, "A printed transition for matching improvement of SIW horn antennas," *IEEE Trans. Antennas Propag.*, vol. 61, no. 4, pp. 1923–1930, Apr. 2013.

[24] M. Esquius-Morote, B. Fuchs, J. Zurcher, and J. R. Mosig, "Novel thin and compact H-plane SIW horn antenna," *IEEE Trans. Antennas Propag.*, vol. 61, no. 6, pp. 2911–2920, Jun. 2013.

[25] L. Wang, M. Esquius-Morote, H. Qi, X. Yin, and J. R. Mosig, "Phase corrected *H*-plane horn antenna in gap SIW technology," *IEEE Trans. Antennas Propag.*, vol. 65, no. 1, pp. 347–353, Jan. 2017.

[26] L. Wang, M. Garcia-Vigueras, M. Alvarez-Folgueiras, and J. R. Mosig, "Wideband H-plane dielectric horn antenna," *IET Microw. Antennas Propag.*, vol. 11, no. 12, pp. 1695–1701, Aug. 2017.

[27] L. Wang, J. L. Gómez-Tornero, and O. Quevedo-Teruel, "Substrate integrated waveguide leaky-wave antenna with wide bandwidth via prism coupling," *IEEE Trans. Microw. Theory Techn.*, vol. 66, no. 6, pp. 3110–3118, Jun. 2018.

[28] Y. J. Cheng, W. Hong, and K. Wu, "Multimode substrate integrated waveguide H-plane monopulse feed," *Electron. Lett.*, vol. 44, no. 2, pp. 78–79, Jan. 2008.

[29] K. Iigusa, K. Li, K. Sato, and H. Harada, "Gain enhancement of H-plane sectoral post-wall horn antenna by connecting tapered slots for millimeter-wave communication," *IEEE Trans. Antennas Propag.*, vol. 60, no. 12, pp. 5548–5556, Dec. 2012.

[30] N. B. Makou, M. S. Sorkherizi, and A. A. Kishk, "Substrate integrated horn antenna loaded with open parallel transitions," *IEEE Antennas Wireless Propag. Lett.*, vol. 16, pp. 349–351, Jun. 2016.

[31] R. Suga, H. Nakano, Y. Hirachi, J. Hirokawa, and M. Ando, "Cost-effective 60-GHz antenna package with end-fire radiation for wireless file-transfer system," *IEEE Trans. Microw. Theory Techn.*, vol. 58, no. 12, pp. 3989–3995, Dec. 2010.

[32] J. Wang *et al.*, "Wideband dipole array loaded substrate integrated H-plane horn antenna for millimeter waves," *IEEE Trans. Antennas Propag.*, vol. 65, no. 10, pp. 5211–5219, Oct. 2017.

[33] M. Esquius-Morote, M. Mattes, and J. R. Mosig, "Orthomode transducer and dual-polarized horn antenna in substrate integrated technology," *IEEE Trans. Antennas Propag.*, vol. 62, no. 10, pp. 4935–4944, Oct. 2014.

[34] Y. Cai, Y. Zhang, Z. Qian, W. Cao, and S. Shi, "Compact wideband dual circularly polarized substrate integrated waveguide horn antenna," *IEEE Trans. Antennas Propag.*, vol. 64, no. 7, pp. 3184–3189, Jul. 2016.

[35] L. Wang, X. Yin, M. Esquius-Morote, H. Zhao, and J. R. Mosig, "Circularly polarized compact LTSA array in SIW technology," *IEEE Trans. Antennas Propag.*, vol. 65, no. 6, pp. 3247–3252, Jun. 2017.

[36] Y.-W. Hsu, T.-C. Huang, H.-S. Lin, and Y.-C. Lin, "Dual-polarized quasi Yagi–Uda antennas with endfire radiation for millimeter-wave MIMO terminals," *IEEE Trans. Antennas Propag.*, vol. 65, no. 12, pp. 6282–6289, Dec. 2017.

[37] Y. Yin, B. Zarghooni, and K. Wu, "Single-layered circularly polarized substrate-integrated waveguide horn antenna array," *IEEE Trans. Antennas Propag.*, vol. 65, no. 11, pp. 6161–6166, Nov. 2017.

[38] S. S. Hesari and J. Bornemann, "Wideband circularly polarized substrate integrated waveguide endfire antenna system with high gain," *IEEE Antennas Wireless Propag. Lett.*, vol. 16, pp. 2262–2265, 2017.

[39] H. Jin, Y. M. Huang, H. Jin, and K. Wu, "*E*-band substrate integrated waveguide orthomode transducer integrated with dual-polarized horn antenna," *IEEE Trans. Antennas Propag.*, vol. 66, no. 5, pp. 2291–2298, May 2018.

[40] V. Rafiei, S. Karamzadeh, and H. Saygin, "Millimetre-wave high-gain circularly polarised SIW end-fire bow-tie antenna by utilising semi-planar helix unit cell," *Electron. Lett.*, vol. 54, no. 7, pp. 411–412, Apr. 2018.

[41] W. E. I. Liu, Z. N. Chen, X. Qing, J. Shi, and F. H. Lin, "Miniaturized wideband metasurface antennas," *IEEE Trans. Antennas Propag.*, vol. 65, no. 12, pp. 7345–7349, Dec. 2017.

[42] S. S. S. Nasser, W. Liu, and Z. N. Chen, "Wide bandwidth and enhanced gain of a low-profile dipole antenna achieved by integrated suspended metasurface," *IEEE Trans. Antennas Propag.*, vol. 66, no. 3, pp. 1540–1544, Mar. 2018.

[43] F. H. Lin, Z. N. Chen, and W. Liu, "A metamaterial-based broadband circularly polarized aperture-fed grid-slotted patch antenna," in *Proc. IEEE Asia–Pacific Conf. Antennas Propag. (APCAP)*, Jun. 2015, pp. 353–354.

[44] F. H. Lin and Z. N. Chen, "Low-profile wideband metasurface antennas using characteristic mode analysis," *IEEE Trans. Antennas Propag.*, vol. 65, no. 4, pp. 1706–1713, Apr. 2017.

[45] F. H. Lin and Z. N. Chen, "Probe-fed broadband low-profile metasurface antennas using characteristic mode analysis," in *Proc. IEEE Asia–Pacific Conf. Antennas Propag. (APCAP)*, Oct. 2017, pp. 664–666.

[46] F. H. Lin and Z. N. Chen, "A method of suppressing higher order modes for improving radiation performance of metasurface multiport antennas using characteristic mode analysis," *IEEE Trans. Antennas Propag.*, vol. 66, no. 4, pp. 1894–1902, Apr. 2018.

[47] F. H. Lin and Z. N. Chen, "Truncated impedance-sheet model for low-profile broadband non-resonant-cell metasurface antennas using characteristic mode analysis," *IEEE Trans. Antennas Propag.*, to be published.

[48] T. Li and Z. N. Chen, "A dual-band metasurface antenna using characteristic mode analysis," *IEEE Trans. Antennas Propag.*, to be published.

[49] T. Li and Z. N. Chen, "Design of dual-band metasurface antenna," in *Proc. IEEE Int. Workshop Antenna Technol. (iWAT)*, Mar. 2018, pp. 1–3.

[50] T. Li and Z. N. Chen, "Design of dual-band metasurface antenna array using characteristic mode analysis (CMA) for 5G millimeter-wave applications," in *Proc. IEEE Antennas Propag. Wireless Commun. (APWC)*, Sep. 2018, pp. 721–724.

[51] T. Li and Z. N. Chen, "Metasurface-based shared-aperture 5G S/K-band antenna using characteristic modes analysis," *IEEE Trans. Antennas Propag.*, to be published.

[52] T. Li, H. Meng, and W. Dou, "Broadband transition between substrate integrated waveguide and rectangular waveguide based on ridged steps," *IEICE Electron. Express*, vol. 11, no. 13, pp. 1–7, Jun. 2014.

[53] R. F. Harrington and J. R. Mautz, "Theory of characteristic modes for conducting bodies," *IEEE Trans. Antennas Propag.*, vol. AP-19, no. 5, pp. 622–628, Sep. 1971.

[54] T. Li and W. Dou, "Broadband right-angle transition from substrate-integrated waveguide to rectangular waveguide," *Electron. Lett.*, vol. 50, no. 19, pp. 1355–1356, Sep. 2014.

[55] R. Glogowski, J.-F. Zurcher, C. Peixeiro, and J. R. Mosig, "Broadband Ka-band rectangular waveguide to substrate integrated waveguide transition," *Electron. Lett.*, vol. 49, no. 9, pp. 602–604, Apr. 2013.

[56] J. Dong, Z. Yang, H. Peng, and T. Yang, "Full Ka-band right-angle transition from substrate integrated waveguide to air-filled rectangular waveguide," *Electron. Lett.*, vol. 51, no. 22, pp. 1796–1798, Oct. 2015.

[57] T. Li, W. Dou, and H. Meng, "Wideband transition between substrate integrated waveguide (SIW) and rectangular waveguide (RWG) based on bend waveguide," in *Proc. Asia–Pacific Microw. Conf. (APMC)*, Nov. 2014, pp. 438–440.

[58] T. Li and W. Dou, "Simple, compact and broadband right-angle transition between substrate integrated waveguide and rectangular waveguide at Ka-band," *Int. J. RF Microw. Comput.-Aided Eng.*, vol. 27, no. 4, p. e21080, Dec. 2016.

Teng Li (M'16) received the B.S. degree from Xiamen University, Xiamen, China, in 2009, and the Ph.D. degree from Southeast University, Nanjing, China, in 2015.

From 2015 to 2016, he was a Post-Doctoral Fellow with Southeast University. In 2016, he joined the Department of Electrical and Computer Engineering, National University of Singapore, Singapore, as a Research Fellow. He has authored or co-authored over 17 journal papers and 15 international conference papers. He holds three granted patents. His current research interests include metamaterials, metasurfaces, characteristic mode analysis, theory of antennas, pattern synthesis, and antenna arrays.

Dr. Li is a Technical Program Committee Member of iWAT2018. He was a recipient of the Best Poster Award at the 2015 International Workshop on Antenna Technology and the 2018 International Workshop on Antenna Technology. He serves on the Reviewer Board for several Journals, including the IEEE TRANSACTIONS ON ANTENNAS AND PROPAGATION, the IEEE ANTENNAS AND WIRELESS PROPAGATION LETTERS, the IEEE MICROWAVE AND WIRELESS COMPONENTS LETTERS, *IET Microwaves Antennas and Propagation*, *Electronics Letters*, the *International Journal of Antennas Propagation*, the *International Journal of Microwave and Wireless Technologies*, *Applied Computational Electromagnetics Society*, and the *Journal of Electromagnetic Waves and Applications*. He also serves as the reviewer for the 2017 Asia–Pacific Conference on Antennas and Propagation.

Zhi Ning Chen (M'99–SM'05–F'07) received the B.Eng., M.Eng., and Ph.D. degrees in electrical engineering from the Institute of Communications Engineering (ICE), Nanjing, China, and the second Ph.D. degree from the University of Tsukuba, Tsukuba, Japan.

From 1988 to 1995, he was a Lecturer and later an Associate Professor with ICE and a Post-Doctoral Fellow and later an Associate Professor with Southeast University, Nanjing. From 1995 to 1997, he was a Research Assistant and later a Research Fellow with the City University of Hong Kong, Hong Kong. From 1999 to 2016, he was a Principal Scientist, the Head of the RF and Optical Department, and a Technical Advisor with the Institute for Infocomm Research (I^2R), Singapore. In 2001 and 2004, he was an Academic Visitor with the IBM T. J. Watson Research Center, Yorktown Heights, NY, USA. In 2012, he joined the Department of Electrical and Computer Engineering, National University of Singapore, Singapore, as a tenured Full Professor, where he is currently the Program Director (industry). In 2013, he visited the Laboratoire des SignauxetSystèmes, UMR8506 CNRS-Supelec-University Paris Sud, Gif-sur-Yvette, France, as a Senior DIGITEO Guest Scientist. He is holding/held the concurrent Guest Professorships with Southeast University (a Changjiang Chair Professor), Nanjing University, Nanjing, Tsinghua University, Beijing, China, Shanghai Jiaotong University, Shanghai, China, Tongji University, Shanghai, University of Science and Technology of China, Hefei, China, Fudan University (an Outstanding Visiting Professor), Shanghai, Dalian Maritime University, Dalian, China, Chiba University, Chiba, Japan, National Taiwan University of Science and Technology, Taipei, Taiwan, Shanghai University (a Ziqiang Professor), Shanghai, Beijing University of Posts and Telecommunications, Beijing, Tohoku University, Sendai, Japan, and City University of Hong Kong (an Adjunct Professor), Hong Kong. He is also serving as the member of the State Key Laboratory of Millimeter-Waves, Southeast University, and City University of Hong Kong. He has authored over 611 academic papers and five books *Broadband Planar Antennas* (Wiley, 2005), *UWB Wireless Communication* (Wiley, 2006), *Antennas for Portable Devices* (Wiley, 2007), *Antennas for Base Stations in Wireless Communications* (McGraw-Hill, 2009), and *Handbook of Antenna Technologies* with 76 chapters as an Editor-in-Chief. He has also contributed the chapters to the books *UWB Antennas and Propagation for Communications, Radar, and Imaging* (Wiley, 2006), *Antenna Engineering Handbook* (McGraw-Hill, 2007), *Microstrip and Printed Antennas* (Wiley, 2010), and *Electromagnetics of Body Area Networks* (Wiley, 2016). He holds 28 granted/filed patents with 35 licensed deals with industry. His current research interests include electromagnetic engineering and antennas/sensors for communication, radar, and imaging and sensing systems.

Dr. Chen elevated a Fellow of the IEEE for the contribution to small and broadband antennas for wireless applications in 2007. He was a recipient of the JSPS Fellowship to conduct his research at the University of Tsukuba in 1997, the International Symposium on Antennas and Propagation Best Paper Award 2010, the CST University Publication Awards 2008 and 2015, the ASEAN Outstanding Engineering Achievement Award 2013, the Institution of Engineers Singapore Prestigious Engineering Achievement Awards 2006, 2013, and 2014, the I^2R Quarterly Best Paper Award 2004, the IEEE iWAT 2005 Best Poster Award, and several technology achievement awards from China from 1990 to 1997 as well as more than 19 academic awards by the students he supervised. He is the founding General Chair of the International Workshop on Antenna Technology (iWAT in 2005), the International Symposium on InfoComm and Mechatronics Technology in BioMedical and Healthcare Application (IS 3Tin3A in 2010), the International Microwave Forum in 2010, and the Asia–Pacific Conference on Antennas and Propagation in 2012. He is also involved many international events as the General Chair, the Chair, and a member of technical program committees and international advisory committees. He has been serving on the IEEE Council on RFID as a Vice President and a Distinguished Lecturer since 2015. He severed as an Associate Editor for the IEEE TRANSACTIONS ON ANTENNAS AND PROPAGATION. He served on the IEEE Antennas and Propagation Society as a Distinguished Lecturer.